

UCSF

UC San Francisco Electronic Theses and Dissertations

Title

Clear Cell Renal Cell Carcinoma: Deep Learning-Based Prediction of Tumor Grade from Contrast-Enhanced CT

Permalink

<https://escholarship.org/uc/item/6xp1q9bv>

Author

Dai, Qing

Publication Date

2019

Peer reviewed|Thesis/dissertation

Clear Cell Renal Cell Carcinoma: Deep Learning-Based Prediction of Tumor Grade
from Contrast-Enhanced CT

by
Qing Dai

THESIS

Submitted in partial satisfaction of the requirements for degree of
MASTER OF SCIENCE

in

Biomedical Imaging


in the

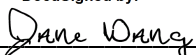
GRADUATE DIVISION

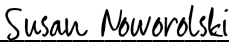
of the

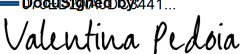
UNIVERSITY OF CALIFORNIA, SAN FRANCISCO

Approved:

DocuSigned by:

1644A2CD853841E... Peder Larson
Chair

DocuSigned by:

DocuSigned by: 417... Jane Wang

DocuSigned by:

DocuSigned by: 441... Susan Noworolski

DocuSigned by:

CB0AB38D57D842C... Valentina Pedoia

Committee Members

Copyright 2019

by

Qing Dai

Clear Cell Renal Cell Carcinoma: Deep Learning-Based Prediction of Tumor Grade from Contrast-Enhanced CT

Qing Dai

Abstract

Tumor grading is an important prognostic parameter for renal cell carcinoma (RCC). However, current grading schemes require an invasive surgical procedure, putting patients at risks including increased risk of hemorrhage, infection, renal failure, or death. Furthermore, low grade RCC is indolent with low mortality risk and may not require treatment. Therefore, a pre-operative and non-invasive assessment of malignancy grade may be beneficial and facilitate optimal timing of treatment. In recent years, deep learning-based image analysis has gained wide popularity in cancer prognosis and prediction. The goal of this study is to investigate the feasibility and performance of a deep-learning-based model for clear cell RCC grading prediction from contrast-enhanced computed tomography (CECT). After institutional review board approval, an institutional pathology database was queried for all renal biopsies between December 2002 and October 2018. All included patients received a CT with a non-contrast and at least one post-contrast series. All patients have Fuhrman grade confirmation from surgical pathology. Tumors were manually annotated by a radiologist on either the corticomedullary or nephrographic phase CECT. Rectangular regions of interest (ROI) were drawn on each slice throughout the tumor and used as inputs to the Deep CNN ResNet50. A low grade or high grade label was assigned to each patient. Sensitivity, specificity, accuracy, and AUC were calculated based on a five-fold cross-validation. Preliminary results from a small subset of data successfully predicted 67% of high-grade clear cell RCCs, and 94% of the low-grade clear cell RCCs.

Table of Contents

| | |
|--|----|
| 1 Introduction | 1 |
| 2 Methods | 6 |
| 2.1 Subjects..... | 6 |
| 2.2 CECT Data Acquisition..... | 6 |
| 2.3 Image Annotation | 8 |
| 2.4 Image Pre-processing and Data Preparation..... | 8 |
| 2.5 Deep Residual Network..... | 9 |
| 2.6 Implementation..... | 10 |
| 2.7 Statistical Analysis | 11 |
| 3 Results | 13 |
| 4 Discussion | 19 |

List of Figures

| | |
|---|----|
| Figure 1 Examples of Different Fuhrman Grading | 2 |
| Figure 2 Contrast Enhancement | 4 |
| Figure 3 Patient Selection Profile | 7 |
| Figure 4 The Image Processing Pipeline | 9 |
| Figure 5 Residual Block | 10 |
| Figure 6 Confusion Matrix | 11 |
| Figure 7. Examples of Receiving Operating Characteristic (ROC) Curves and Area Under the Curve (AUC)..... | 12 |
| Figure 8 Renal Tumor Subtypes..... | 14 |
| Figure 9 Confusion Matrices..... | 17 |
| Figure 10 Receiving Operating Characteristics..... | 18 |

List of Tables

| | |
|---|----|
| Table 1 Fuhrman Grading Criteria | 3 |
| Table 2 Contrast-enhanced CT Acquisition Protocol..... | 4 |
| Table 3 Cohort Characteristics | 15 |
| Table 4 Characteristics of a preliminary subset..... | 16 |
| Table 5 Performance of the Models..... | 17 |

1. Introduction:

Renal cancer is the sixth and eighth most common cancer type in men and women respectively in United States with more than 73,800 new cases every year (American Cancer Society). Renal cell carcinoma (RCC), accounts for 90% of renal cancers. Since 1975, the incidence rate of renal cancer doubled from 7.1 per 100,000 to 15.5 per 100,000, while the mortality remained constant (National Cancer Institute). Part of this rise is likely due to the use and development of newer imaging techniques, including computed tomography (CT), magnetic resonance imaging (MRI) and ultrasonography (US) (Sasaguri and Takahashi; Vedanayagam et al.; Herts et al.; Dunlop and Cohen). Given that kidneys are positioned deep within the body and cannot be palpated on a physical exam, renal tumors often have no signs or symptoms at an early stage. Most of the renal cancers are actually found incidentally from imaging tests for a different clinical indication (Herts et al., 2018; Sasaguri & Takahashi, 2018; Vedanayagam, Bhattacharya, & Sriprasad, 2017).

Tumor grading is an important prognostic parameter for renal cancers. Low grade indicates that cancer cells are growing slowly, while high grade indicates that the cancer cells are growing quickly and are more likely to spread. The most popular grading scheme for renal cancers is called Fuhrman grading (Fuhrman et al.), which is based on three nuclear morphological parameters of the pathological materials: nuclear size, nuclear shape, and nucleolar prominence (Table 1). Examples of different grades are shown in Figure 1. The Fuhrman grading system has been validated to demonstrate strong prognostic value. However, pathological tumor grading requires an invasive surgical procedure, which is associated with risk of hemorrhage, infection, renal failure, or death. Given that benign renal tumors and many small RCCs demonstrate slow

growth and low metastatic potentials, a pre-operative assessment of tumor grade could risk stratify patients before surgery.

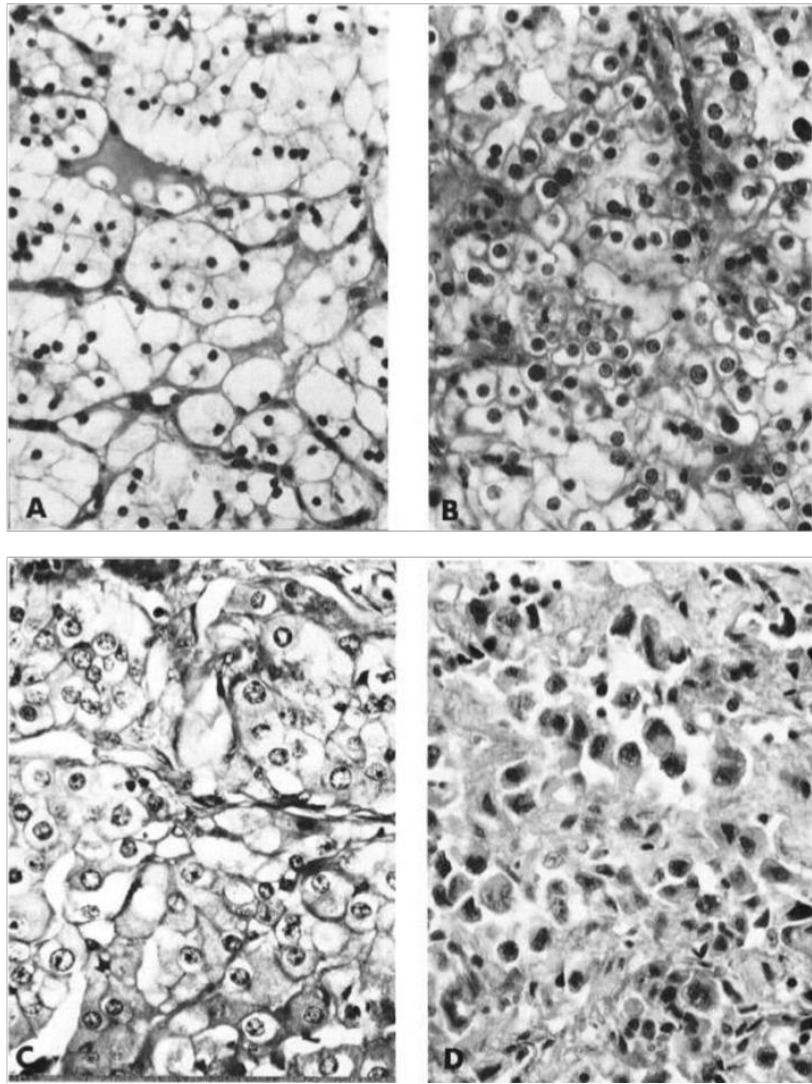


Figure 1, Examples of different Fuhrman grading. Grade 1-4, A-D.

Table 1. Fuhrman grading criteria.

| | Nuclear size | Nuclear Shape | Nucleoli |
|---------|--|---|---|
| Grade 1 | Small (approximately 10 μ m) | Round and uniform | Absent or inconspicuous |
| Grade 2 | Larger (approximately 15 μ m) | Slightly irregular in outlines | Frequently visible at high power (400X) |
| Grade 3 | Even larger nuclei (approximately 20 μ) | Obvious irregular outlines | Prominent and large at low power (100X) |
| Grade 4 | Similar to grade 3 | Extremely irregular outlines, bizarre and multilobed shapes | Conspicuous nucleoli |

Diagnostic medical imaging is the standard of care for pre-operative tumor characterization and staging and CT scan is the preferred imaging modality to evaluate renal masses. CT scan measures the average X-ray attenuation coefficient of a tissue voxel, and the attenuation coefficient is then translated and normalized to Hounsfield Units (HU) from the following equation:

$$HU = 1000 \times \frac{\mu - \mu_{water}}{\mu_{water} - \mu_{air}}$$

where μ , μ_{water} and μ_{air} are the attenuation coefficients of a tissue voxel, water and air. The CT pixel value is display on a scale from -1024 to +3071 in HU units. Water and air are 0 and -1000 in HU scale. For renal masses characterization, a homogenous lesion with >70 HU is usually considered as a hemorrhagic cyst, and a lesion with < -20 HU is usually considered as a benign tumor subtype or a proteinaceous cyst.

Contrast-enhanced CT (CECT) is most commonly used for RCC detection and characterization. The purpose of CECT is to better visualize the lesions by enhancing their

contrast from the healthy surrounding tissues (Figure 2). After intravenous injection of a contrast agent, the lesion has different enhancement characteristics at different phases, so the timing of postcontrast CT acquisition is important (Table 2). For clear cell RCC, the high vascular structure often exhibits a strong enhancement in the late-arterial phase. If the lesion is small, the mass may be more conspicuous in portal venous phase, which also has a strong enhancement (Dyer et al.).

| Contrast-enhanced CT | Time (second) |
|----------------------|-----------------------------|
| Pre-contrast | 0 sec, during expiration |
| Late Arterial | 40 sec, during expiration |
| Portal venous | 80 sec, during expiration |
| Delayed | >100 sec, during expiration |

Table 2: Contrast-enhanced CT Acquisition Protocol. This is the standard protocol for renal masses at our institution.

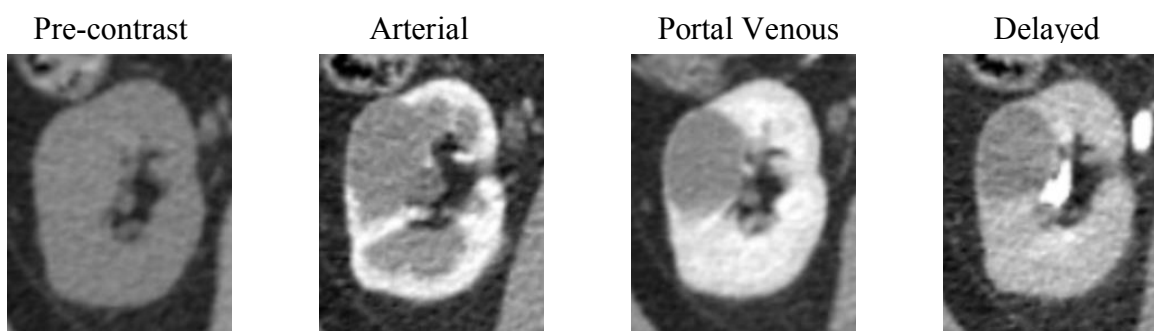


Figure 2 Contrast enhancement. This figure shows a four-phase CECT scan of a patient with a single renal mass in the right kidney.

Machine learning is widely used for developing automate medical imaging workflows. Conventional machine learning (ML) techniques aim to select and extract hand-crafted features from imaging data. This method has been applied to many investigations, such to predict renal tumor subtypes and malignancy (Sasaguri and Takahashi; Yu et al.; Huhdanpaa et al.; Ding et al.). However, the performance of conventional ML models relies heavily on the quality of those hand-crafted features to be extracted and is not reliable due to the variance among different datasets. In recent years, deep neural networks have shown promising results in every field of medical imaging (Havaei et al.; Zhang et al.; Zhou et al.; Coy et al.; Han et al.). Compare to conventional ML models, deep neural network models act as a generic feature extractor, learning directly from input not from human experts.

Two approaches are commonly used to train a deep neural network: train from scratch and transfer learning. Train from scratch is a method where all the parameters of a model are randomly initialized and are fully optimized to a specific dataset. However, the performance of training a model from scratch may be constrained by over-fitting (model fitted too close to a limited dataset) and data imbalance (a disproportionate ratio between class observations). Medical imaging data is inherently suffered from both of these two problems. Transfer learning is a method where a model developed and optimized for a task is reused on a second task. With transfer learning, a pre-trained model is used as a starting point followed by fine tuning using the desired dataset. Tajbakhsh et al. showed that fine-tuned deep neural networks outperformed fully trained models when limited data were available (Tajbakhsh et al.).

The goal of this study is to investigate the feasibility and performance of a deep neural network-based clear cell RCC grading prediction model from CECT. A preliminary study using a small dataset is reported here.

2. Methods

2.1 Subjects

After institutional review board approval, we searched for patients with biopsy proven RCC were identified from radiology, pathology and clinical databases. A summary of patient selection criteria is shown in Figure 3. Only patient with stage 1 cancers were included for this study. Patients with obvious local invasion to neighboring tissues or distant metastases were excluded from this study. Patients with obvious metastases were also excluded. All patients obtained CECT with at least one pre-contrast acquisition scan and one contrast-enhanced acquisition. Surgical pathology results were available for all tumors from image-guided percutaneous biopsies, partial nephrectomy or radical nephrectomy. A unique histological grade was assigned to each histologic material based on Fuhrman grading system. Patients with surgery performed prior to baseline imaging scans were excluded.

2.2 CECT Data Acquisition:

Our institutional Renal Mass Protocol is described as follows: Helical CT scans were obtained with a gantry rotation speed of 0.5 rotations/second, table speed at 39.37mm/rot, tube voltage of 120 kVp, min/max tube current of 150/570 mA, and beam pitch of 0.984:1. The scan was first acquired at slice thickness of 1.25mm, then reformatted automatically in axial (2.5mm), sagittal (5mm) and coronal (3mm) planes and sent to a picture archiving and communication system (PACS). Reformatted images had sizes of 512x512 with pixel spacing of 0.9765mm. Following pre-contrast scans, 150cc non-ionic contrast agents (Omnipaque 350) was administrated through IV injection at 5ml/s followed by a 50-cc saline flush.

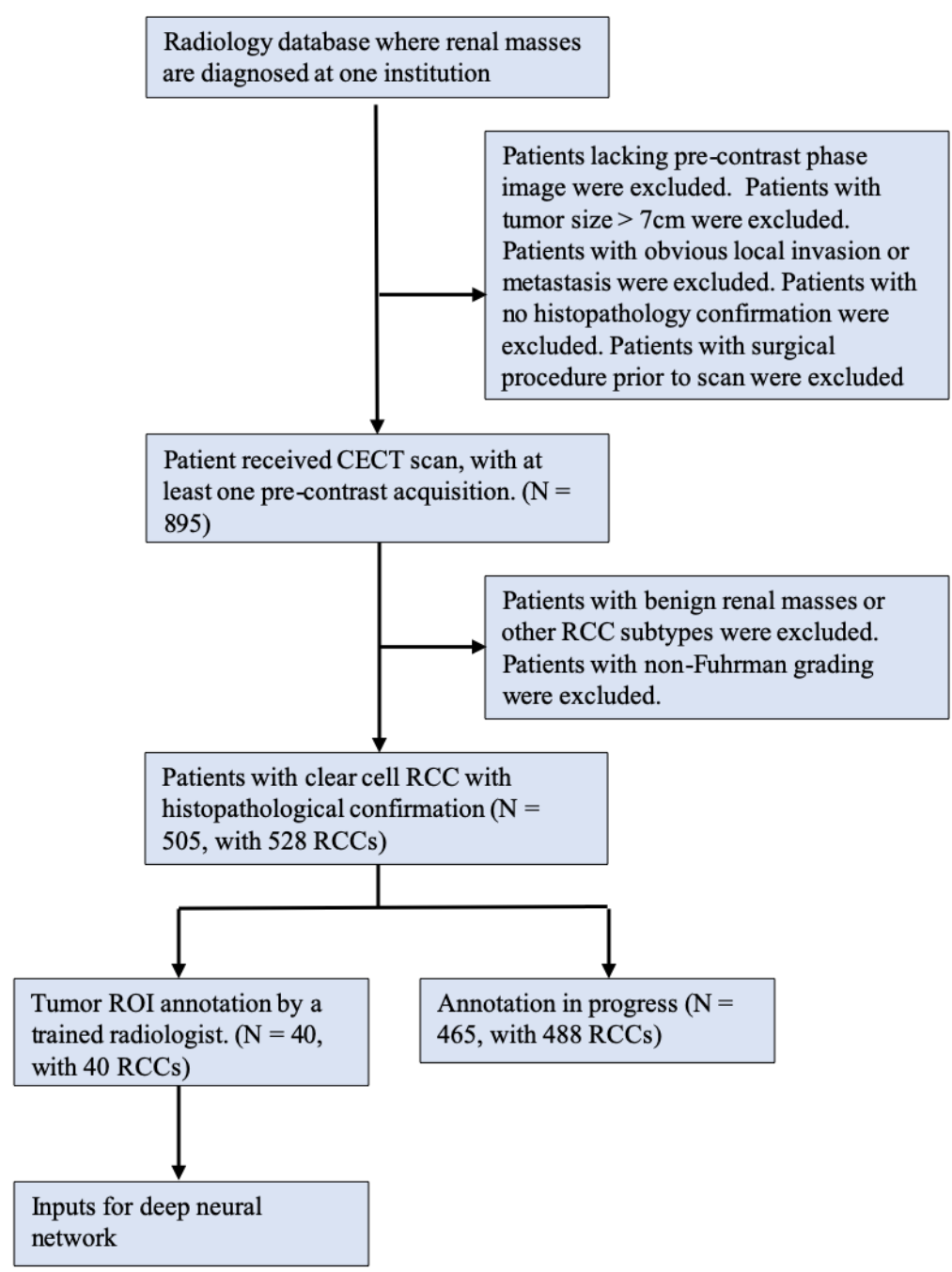


Figure 3 Patient selection profile.

2.3 Image Annotation

All CECT exams were automatically retrieved from PACS in DICOM format in a 1996 Health Insurance Portability and Accountability Act (HIPAA) compliant manner. Tumor ROIs were labeled on MD.ai (New York, New York, United States), a cloud-based collaborative annotation platform that allows the storage, viewing and annotation of anonymized medical images. Tumor ROIs were drawn manually using a polygon tool on the late arterial or portal-venous phase axial images depending on where the tumor was more conspicuous. XY coordinates of the vertices of the polygons were saved and exported as a .json file.

2.4 Image Pre-processing and Data Preparation

The DICOM images were in HU unit and ranged from -1024 to 3071 with a soft tissue window (window center 40, window width 400). Based on the vertices, square bounding boxes with size 128x128 were automatically generated with tumor centroid in the center. Image was then cropped from 512x512 to 128x128. Random left-right flips is applied to augment the datasets to increase the diversity of the datasets for model training.

Transfer learning was used in this study. For the used by a pre-trained neural network, two additional image processing were performed: First the images were converted from grayscale images to 3-channel images by duplication and concatenation. Second, the image were resized from 128x128 to 224x224, because the height and the width were expected to be at least 224x224. Final input dimensions for model training were 224x224x3. A five-fold cross-validation was applied with an 80/20 split at the patient level. All slices were shuffled at the beginning of each training/validation split.

Image annotation and processing steps are illustrated in Figure 4. Image processing was performed using Pydicom 1.3.0 and pynrrd 0.4.0, respectively. Image transformation and augmentation were performed using Dataset class and transforms.functional module provided in Pytorch v1.1.0 .

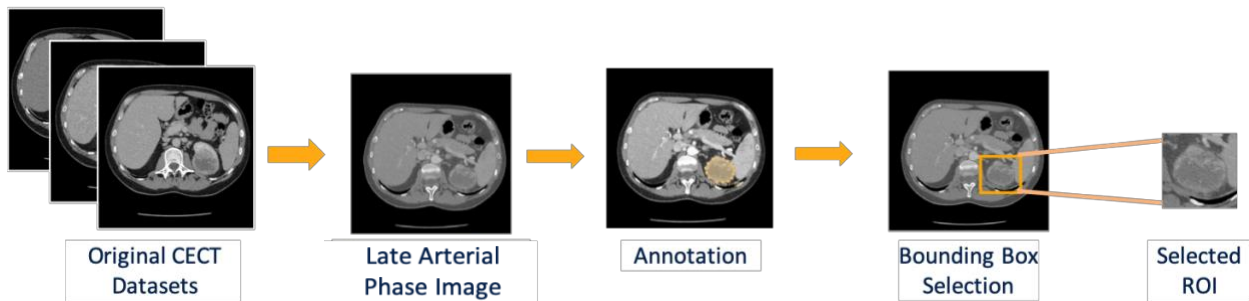


Figure 4 The image processing pipeline. Original CECT datasets were retrieved from PACS in DICOM format. Late arterial or portal venous phase were selected based on series instance UID stored in DICOM headers. Annotation was performed using a polygon tool. A 128x128 bounding box was generated and cropped. Annotation was performed on MD.ai. Image processing was performed in python 3.6.

2.5 Deep Residual Network

A residual neural network (ResNet) architecture was used for model training (He et al.). First introduced in 2015, the core idea of ResNet is to add “shortcut connections” between layers within a residual block. Instead of simply stacking layers and learning from the outputs of the previous layers, residual blocks (as shown in Figure 5) allow the model to skip certain layers and directly learn an identity function X by setting the residual $\mathcal{F}(x, \{W_i\})$ to zero in the following equation:

$$y = \mathcal{F}(x, \{W_i\}) + x \quad (2)$$

where x is the input of this residual block, W_i is the weights to be updated in this residual block, and y is the output of this residual block. Adding residual blocks minimizes the gradient vanishing problem, giving us the ability to train a deeper network.

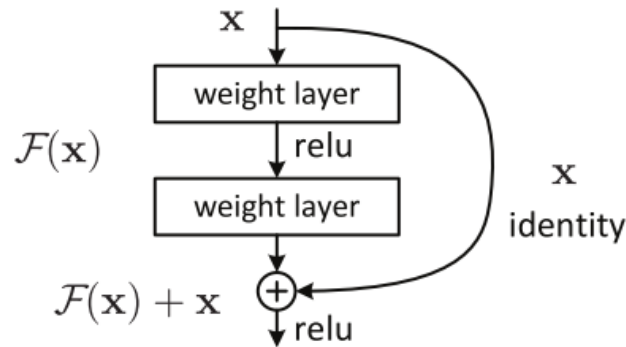


Figure 5 Residual Block. (He et al.)

2.6 Implementation

Given the limited data available for training, we used transfer learning to train our classification model. In this study, a ResNet 50 model was pre-trained on ImageNet datasets, which contains over 1 million images from 1000 classes (Russakovsky et al.). Only the last two residual layers were trained, and the first two residual layers were frozen with fixed parameters. The final layer was a classifier that performed a binary classification: 0 for low grade (Fuhrman grade 1 or 2) and 1 for high grade (Fuhrman grade 3 or 4). Adaptive Momentum (Adam) optimization was used for parameter updating (Kingma and Ba). Learning rate was set to $1e-5$, learning rate momentum = 0.8, weight decay = 0.8. A weighted cross-entropy loss was used with a weight = 2.5. The model was developed in Pytorch v1.1.0 and trained on NVIDIA Titan X Pascal GPU with 12GB memory.

2.7 STATISTICAL ANALYSIS

Since our model performs a binary classification, we define the following term:

- True positives (TP) are cases where the model predicted high grades (label 1), and they do have high grades (label 1);
- False positives (FP) are cases where model predicted high grades (label 1), but they are low grades (label 0);
- False negatives (FN) are cases where model predicted low grade (label 0), but they are high grades (label 1);
- True negatives (TN) are cases where model predicted low grades (label 0), and they are low grades (label 0).

We used confusion matrices to visualize the above terms (Figure 6).

| | | Actual Values | |
|------------------|--------------|---------------|--------------|
| | | Positive (1) | Negative (0) |
| Predicted Values | Positive (1) | TP | FP |
| | Negative (0) | FN | TN |

Figure 6. Confusion matrix.

Sensitivity, specificity and accuracy are comparison metrics commonly used in medical tests. Sensitivity measures how well the test identifies those with positive conditions, specificity measure how well the test identifies those with negative conditions, and accuracy measures how

well the test identifies both negative and positive conditions. Sensitivity, specificity and accuracy can be calculated from the following equations:

$$\text{Sensitivity} = \frac{TP}{TP+FN} \quad (3)$$

$$\text{Specificity} = \frac{TN}{TN+FP} \quad (4)$$

$$\text{Accuracy} = \frac{TP+TN}{TP+TN+FP+FN} \quad (5)$$

A receiving operating characteristic (ROC) curve measures how good a binary classification model can distinguish two classes. A ROC curve plots sensitivity vs 1-specificity at different classification thresholds. Area under the curve (AUC) also measures how the performance of the model distinguishes the positives and the negatives. A perfect classifier has AUC of 1, while a random classifier has AUC of 0.5. (Figure 7)

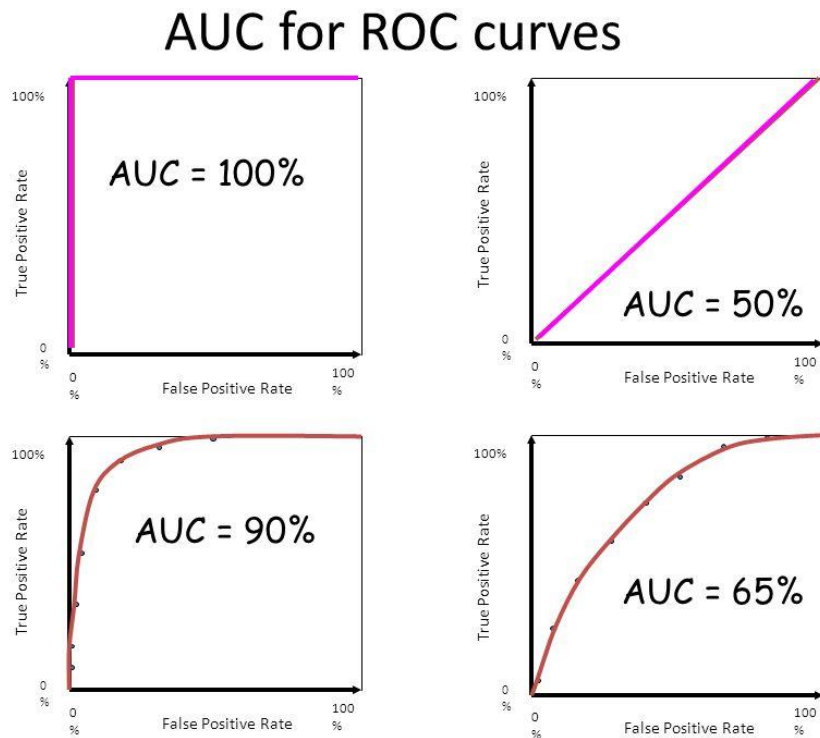


Figure 7. Examples of receiving operating characteristic (ROC) curves and area under the curve (AUC).

3 Results

Out of 895 patients with renal tumors, 505 patients with 528 lesions were diagnosed as clear cell RCCs. These proportions (56.4% of all tumors, 73.7% of all RCCs) were close to the numbers reported in previous studies (Figure 8) (Davenport et al.). Among all patients with clear cell RCCs, 50 were grade 1, 311 were grade 2, 120 were grade 3, and 24 were grade 4. 361 (71.5%) patients were categorized to low grade (grade 1 or 2) and 144 (28.5%) were categorized to high grade (grade 3 or 4). Table 3 showed the characteristics of the entire cohort.

Table 4 showed a subset of the complete population that were analyzed in this preliminary study. Annotation were performed on 40 patients with 40 clear cell RCCs, 26 with high grade clear cell RCC tumors and 14 with low grade clear cell RCC tumors. The mean size of the lesions was 4.10 cm (standard deviation, 1.52cm; range, 1.1 – 6.7 cm).

Table 5 summarized the performances of our deep residual networks. We explored the impact of 3 different batch sizes to the performance. The total number of trainable parameters was approximately 11 million. The best performing model achieved 0.67 for sensitivity, 0.94 for specificity, 0.84 for accuracy, 0.0.88 for AUC. Confusion matrices and receiver operating characteristics (ROC) curves were shown in Figure 9 and Figure 10.

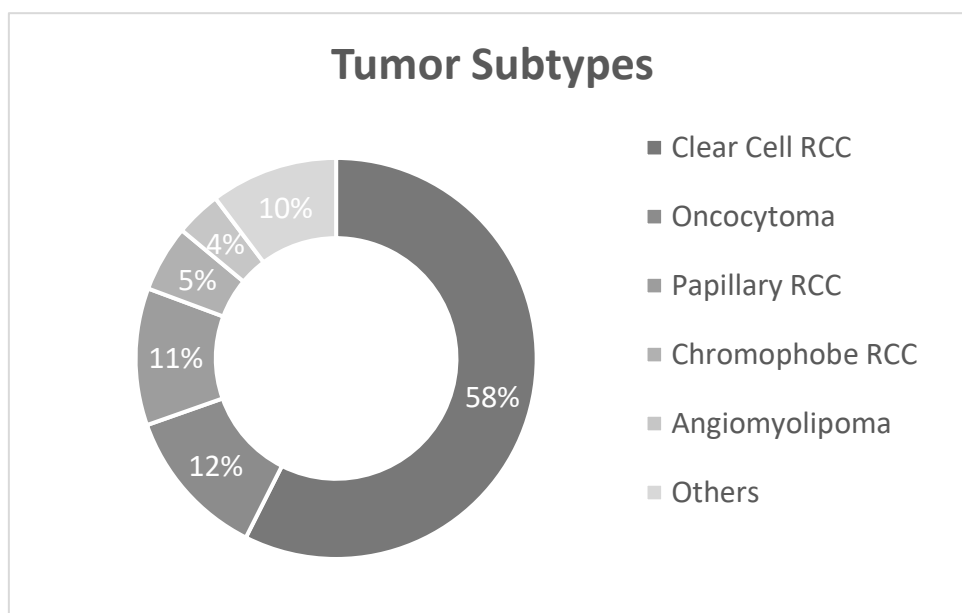


Figure 8 Renal Tumor Subtypes. Among all 895 patients identified with renal tumor, 514 (58%) had clear cell RCCs, 109 (12%) had oncocytoma, 99 (11%) had papillary RCC, 48 (5%) had chromophobe RCC, 33 (4%) had angiomyolipoma, 92 (10%) had mixed type tumor or tumor type unclassified.

Table 3 Cohort characteristics. the cohort comprises contains 505 patients with 528 clear cell RCCs. Note each tumor is counted separately if bilateral tumors or multiple tumors are presented.

| | Low Grade, N = 361 | High Grade, N = 144 | Total, N = 505 |
|-----------------------|---------------------------|----------------------------|-----------------------|
| Contrast phase | | | |
| Non-contrast | 361 (100%) | 143 (99.3%) | 504 (99.8%) |
| Late arterial | 169 (46.8%) | 53 (36.8%) | 222 (43.0%) |
| Portal venous | 319 (88.4%) | 128 (88.9%) | 447 (88.5%) |
| Delayed | 229 (63.4%) | 89 (61.8%) | 318 (63.0%) |
| Procedure type | | | |
| Biopsy | 61 (16.9%) | 14 (9.7%) | 75 (14.8%) |
| Partial Nephrectomy | 199 (55.1%) | 77 (53.5%) | 276 (54.7%) |
| Radical Nephrectomy | 101 (28.0%) | 53 (36.8%) | 154 (30.5%) |
| Laterality | | | |
| Left | 182(50.4%) | 76 (52.8%) | 258 (51.1%) |
| Right | 170 (47.1%) | 66 (45.8%) | 236 (46.7%) |
| Bilateral | 9 (2.5%) | 2 (1.4%) | 11 (2.2%) |
| Size | | | |
| Mean, Std (cm) | 3.80 ± 1.57 | 4.66 ± 1.59 | 4.04 ± 1.62 |
| Range (cm) | 1 - 7 | 1.7 – 7 | 1 - 7 |

Table 4 Characteristics of a preliminary subset, containing 40 patients with 40 clear cell RCCs.

| | Low Grade, N = 24 | High Grade, N = 16 | Total, N = 40 |
|-----------------------|--------------------------|---------------------------|----------------------|
| Procedure type | | | |
| Biopsy | 6 (25%) | 2 (12.5%) | 6 (15%) |
| Partial Nephrectomy | 16 (33.7%) | 8 (50%) | 24 (60%) |
| Radical Nephrectomy | 4 (16.7%) | 6 (37.5%) | 10 (25%) |
| Laterality | | | |
| Left | 10 (41.7%) | 9 (52.8%) | 19 (47.5%) |
| Right | 16 (66.7%) | 4 (45.8%) | 20 (50%) |
| Bilateral | 0 (0%) | 1(1.4%) | 1 (2.5%) |
| Size | | | |
| Mean, Std (cm) | 3.83 ± 1.48 | 4.41 ± 1.71 | 4.04 ± 1.57 |
| Range (cm) | 1.1 – 6.3 | 1.8 - 6.7 | 1.1 – 6.7 |

Table 5 Performance of the models. Batch size with 16 reached the best sensitivity, specificity and accuracy

| | Sensitivity | Specificity | Accuracy |
|-----------------|-------------|-------------|----------|
| Batch Size = 4 | 0.55 | 0.88 | 0.77 |
| Batch Size = 16 | 0.67 | 0.94 | 0.84 |
| Batch Size = 64 | 0.53 | 0.81 | 0.71 |

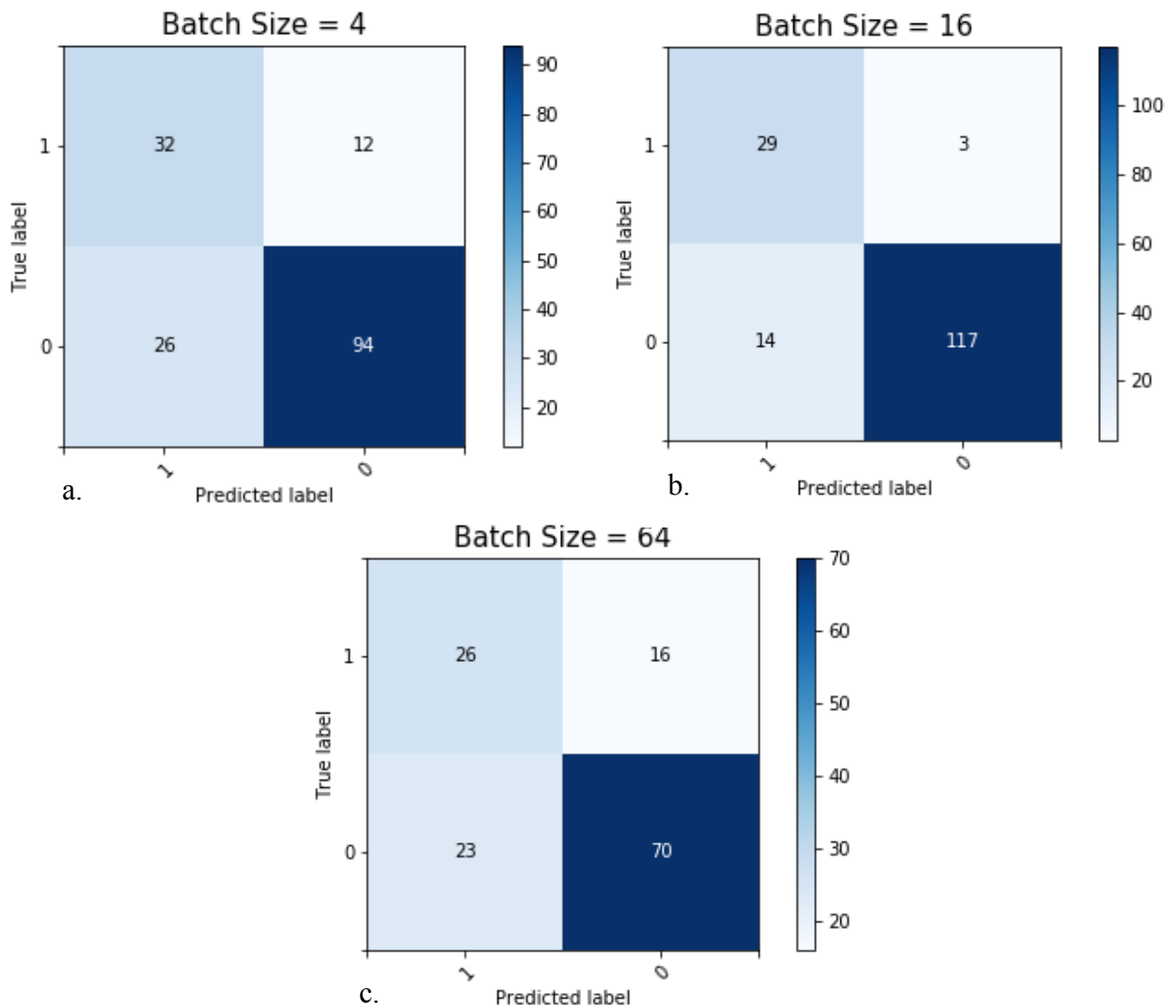


Figure 9 Confusion matrices. Results for batch size of 4, 16, and 64 are shown. True positives are shown at the top-left corner, false negatives at top-right corner, false positives at bottom-left corner, and true negatives at bottom-right corner.

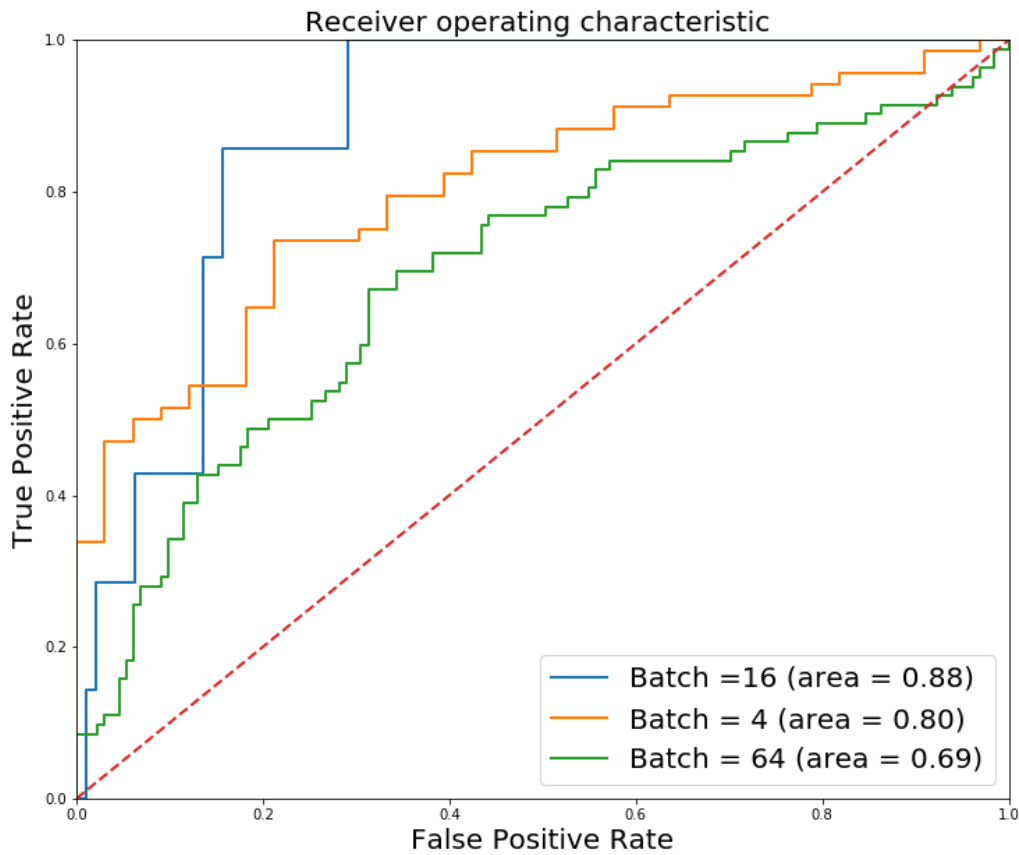


Figure 10 Receiving Operating Characteristics. Areas under the curve are shown in the legends. Batch size of 16 reached the best AUC value, which is consistent with Table 4.

4 Discussion

We presented a deep learning-based framework for pre-operative pathological grade prediction of clear cell RCC from CECT imaging. Our model successfully predicted 67% of high-grade clear cell RCCs, and 94% of the low-grade clear cell RCCs.

As far as we know, no previous study has used deep neural network to discriminate low and high Fuhrman grading. Several works used conventional machine learning for this task: Ding et al. used six non-texture features (diameters, absolute and relative enhancement, etc.) and four texture features (out of 184 texture features) from CECT imaging, and a logistic regression model was used for prediction (Ding et al.); Bektas et al. used additional texture features, such as gradient features, image nonuniformities, wavelet features, etc., and more classifiers were investigated (Bektas et al.). Both studies proved CECT provided enough predictive information for RCC classification and grading. However, both studies required hand-crafted feature selection schemes which lacked generalizability.

The use of deep learning on RCC classification has been validated on CECT dataset for similar tasks: Coy et al. used a pre-trained Google Inception model to differentiate between clear cell RCC and its benign mimics (Coy et al.). Han et al. also used a pre-trained Google Inception model to distinguish three major subtypes of RCCs on three-phase CECT images (Han et al.).

The generalization of this study is subject to several considerations. First is data scarcity. The patient selection criteria of this study were narrow, and the number of patients included in this preliminary study was small ($N = 40$). We addressed this by augmenting our training datasets, as well as ensuring that class proportion of our training datasets was similar to the complete cohort and populations in other studies. We didn't balance the data because we wanted

the model to see an accurate representation of the class proportion in reality. Also, the clinical characteristics of these 40 patients was similar to the full datasets.

Second is bias. The ground truth provided by pathology for training may be biased from sampling errors or from pathology readers. Further, the annotation provided by our radiologist may similarly be inaccurate due to reader bias and variability. We can recruit more readers to perform annotation and measure inter-reader variability in further investigation.

Some future directions of this study include: The full 895 patient dataset (12 times more) will be used for model development as soon as it is annotated; alternative networks will be explored, such as Google Inception or 3D networks.

In conclusion, the work presented here demonstrated a deep learning-based model was useful to capture the difference between low- and high-grade clear cell RCCs. Given the important clinical implication of a pre-operative pathological grade prediction, this could lead to a paradigm shift in the management of renal cancers in the future with improved optimization of the timing of interventions.

References:

American Cancer Society. *Cancer Facts & Figures 2019*. 2019.

Bektas, Ceyda Turan, et al. “Clear Cell Renal Cell Carcinoma: Machine Learning-Based Quantitative Computed Tomography Texture Analysis for Prediction of Fuhrman Nuclear Grade.” *European Radiology*, vol. 29, no. 3, European Radiology, 2019, pp. 1153–63, doi:10.1007/s00330-018-5698-2.

Coy, Heidi, et al. “Deep Learning and Radiomics: The Utility of Google TensorFlow™ Inception in Classifying Clear Cell Renal Cell Carcinoma and Oncocytoma on Multiphasic CT.” *Abdominal Radiology*, vol. 44, no. 6, Springer US, 2019, pp. 2009–20, doi:10.1007/s00261-019-01929-0.

Davenport, Matthew S., et al. “Diagnosis of Renal Angiomyolipoma with Hounsfield Unit Thresholds: Effect of Size of Region of Interest and Nephrographic Phase Imaging.” *Radiology*, vol. 260, no. 1, July 2011, pp. 158–65, doi:10.1148/radiol.11102476.

Ding, Jiule, et al. “CT-Based Radiomic Model Predicts High Grade of Clear Cell Renal Cell Carcinoma.” *European Journal of Radiology*, vol. 103, no. February, Elsevier, 2018, pp. 51–56, doi:10.1016/j.ejrad.2018.04.013.

Dunlop, Joan H., and Joanna S. Cohen. “Incidental Renal Mass Found on Focused Assessment with Sonography in Trauma.” *Pediatric Emergency Care*, vol. 30, no. 10, Lippincott Williams and Wilkins, 12 Oct. 2014, pp. 752–54, doi:10.1097/PEC.0000000000000242.

Dyer, Ray, et al. “Simplified Imaging Approach for Evaluation of the Solid Renal Mass in Adults.” *Radiology*, vol. 247, no. 2, May 2008, pp. 331–43, doi:10.1148/radiol.2472061846.

Fuhrman, S. A., et al. “Prognostic Significance of Morphologic Parameters in Renal Cell Carcinoma.” *American Journal of Surgical Pathology*, vol. 6, no. 7, 1982, pp. 655–63.

- Han, Seokmin, et al. "The Classification of Renal Cancer in 3-Phase CT Images Using a Deep Learning Method." *Journal of Digital Imaging*, Journal of Digital Imaging, 2019, pp. 638–43, doi:10.1007/s10278-019-00230-2.
- Havaei, Mohammad, et al. "Brain Tumor Segmentation with Deep Neural Networks." *Medical Image Analysis*, vol. 35, Elsevier B.V., 2017, pp. 18–31, doi:10.1016/j.media.2016.05.004.
- He, Kaiming, et al. "Deep Residual Learning for Image Recognition." *Proceedings of the IEEE Computer Society Conference on Computer Vision and Pattern Recognition*, vol. 2016-Decem, 2016, pp. 770–78, doi:10.1109/CVPR.2016.90.
- Herts, Brian R., et al. "Management of the Incidental Renal Mass on CT: A White Paper of the ACR Incidental Findings Committee." *Journal of the American College of Radiology*, vol. 15, no. 2, Elsevier B.V., Feb. 2018, pp. 264–73, doi:10.1016/j.jacr.2017.04.028.
- Huhdanpaa, Hannu, et al. "CT Prediction of the Fuhrman Grade of Clear Cell Renal Cell Carcinoma (RCC): Towards the Development of Computer-Assisted Diagnostic Method." *Abdominal Imaging*, vol. 40, no. 8, Springer US, 2015, pp. 3168–74, doi:10.1007/s00261-015-0531-8.
- Kingma, Diederik P., and Jimmy Ba. *Adam: A Method for Stochastic Optimization*. Dec. 2014, <http://arxiv.org/abs/1412.6980>.
- National Cancer Institute. *SEER Cancer Stat Facts: Kidney and Renal Pelvis Cancer*. 2017.
- Russakovsky, Olga, et al. "ImageNet Large Scale Visual Recognition Challenge." *International Journal of Computer Vision*, vol. 115, no. 3, Springer US, 2015, pp. 211–52, doi:10.1007/s11263-015-0816-y.
- Sasaguri, Kohei, and Naoki Takahashi. "CT and MR Imaging for Solid Renal Mass Characterization." *European Journal of Radiology*, 2018, doi:10.1016/j.ejrad.2017.12.008.

- Tajbakhsh, Nima, et al. “Convolutional Neural Networks for Medical Image Analysis: Full Training or Fine Tuning?” *IEEE Transactions on Medical Imaging*, vol. 35, no. 5, Institute of Electrical and Electronics Engineers Inc., May 2016, pp. 1299–312, doi:10.1109/TMI.2016.2535302.
- Vedanayagam, M., et al. “Magnetic Resonance Imaging and the Use in Small Renal Masses.” *Indian Journal of Surgical Oncology*, vol. 8, no. 1, Springer India, 1 Mar. 2017, pp. 19–23, doi:10.1007/s13193-016-0575-4.
- Yu, Hei Shun, et al. “Texture Analysis as a Radiomic Marker for Differentiating Renal Tumors.” *Abdominal Radiology*, vol. 42, no. 10, Springer US, 2017, pp. 2470–78, doi:10.1007/s00261-017-1144-1.
- Zhang, Qi, et al. “Deep Learning Based Classification of Breast Tumors with Shear-Wave Elastography.” *Ultrasonics*, vol. 72, Elsevier B.V., 2016, pp. 150–57, doi:10.1016/j.ultras.2016.08.004.
- Zhou, Leilei, et al. “A Deep Learning-Based Radiomics Model for Differentiating Benign and Malignant Renal Tumors.” *Translational Oncology*, vol. 12, no. 2, The Authors, 2019, pp. 292–300, doi:10.1016/j.tranon.2018.10.012.

Publishing Agreement

It is the policy of the University to encourage the distribution of all theses, dissertations, and manuscripts. Copies of all UCSF theses, dissertations, and manuscripts will be routed to the library via the Graduate Division. The library will make all theses, dissertations, and manuscripts accessible to the public and will preserve these to the best of their abilities, in perpetuity.

Please sign the following statement:

I hereby grant permission to the Graduate Division of the University of California, San Francisco to release copies of my thesis, dissertation, or manuscript to the Campus Library to provide access and preservation, in whole or in part, in perpetuity.



Author Signature

9/5/19.

Date